

外文文献翻译

应用物理 15-1 班 张凡

基于数字摩尔的光学 3D 测量：像素级别校准，去除格状噪声，和时间相位展开

第五章：二图片和三图片时间相位展开

在这一章，二图片和三图片数字摩尔时间相位展开被提出分别计算一个精确的使用 2 个或者 3 个不同频率的条纹投影产生的连续相位映射。这一方法需要将一个单独二值条纹的投影，然后为每一个条纹频率捕捉图片来计算折叠的相位，但是相位移动出现在捕捉图片后的过程。相位移动分析能得出不同摩尔波长的相位映射。计算每个相位的摩尔波长需要在系统校准中使用有噪声的相位映射作为参考来展开较短波长的相位映射。这使得使用较条纹投影方法少的图片完成精确连续位相的计算。

5.1 数字相位移动摩尔

这一使用多波长数字相位移动摩尔的时间相位展开方法需要将多个不同频率的投影到物体表面，然后对于每一个（不同摩尔频率）的捕捉到的图片，一个合成的（由计算机生成的）相同频率重合在捕捉到的图片上，然后数字移动，生成多个相位移动的摩尔条纹。第三章详细提到此方法。

生成的相位移动的摩尔条纹包含这摩尔等高线和不需要的高频条纹图样。接下来条纹去除方法用来去除纯条纹。第四章详细提到此方法。在去除条纹后，相位移动摩尔图样的强度分布有以下公式描述：

$$I_i = a(x, y) + b(x, y)\cos(\Phi(x, y) + \delta_i), \quad (5.1)$$

其中 $a(x, y)$ 和 $b(x, y)$ 分别是背景和调制强度， (x, y) 是图像像素坐标。 $\Phi(x, y)$ 是相位对应物体高度信息的映射， $\delta_i = 2\pi i / N$ 是图像之间的相位移动。为了计算相位映射 $\Phi(x, y)$ ，至少需要三张图片 ($N = 3$) 的相位摩尔图样：

$$\Phi(x, y) = -\tan^{-1}\left(\frac{\sum_{i=1}^N I_i(x, y) \sin \delta_i}{\sum_{i=1}^N I_i(x, y) \cos \delta_i}\right), i = 1, 2, \dots, N. \quad (5.2)$$

由于在公式 5.2 里反三角函数，计算所得的相位是折叠在 $[\pi, -\pi]$ ，并且由于一个二维的相位展开方法需要来去计算连续的相位映射 $\Phi(x, y)$ 。这一过程根据条纹的级数 $m(x, y)$ 去除折叠相位的 2π 的不确定性。

$$\varphi(\mathbf{x}, \mathbf{y}) = \Phi(\mathbf{x}, \mathbf{y}) + (2\pi)\mathbf{m}(\mathbf{x}, \mathbf{y}) \quad (5.3)$$

展开相位和物体高度之间的关系取决于系统几何参数，这一关系有以下公式描述：

$$\mathbf{h}(\mathbf{x}, \mathbf{y}) = \mathbf{K}\varphi(\mathbf{x}, \mathbf{y}) \quad (5.4)$$

系数 \mathbf{K} 是关于条纹波长 λ 的函数：

$$\mathbf{K} = \frac{\lambda}{2\pi} \quad (5.5)$$

公式 5.4 可以被写成：

$$\mathbf{h}(\mathbf{x}, \mathbf{y}) = \frac{\lambda}{2\pi} (\varphi(\mathbf{x}, \mathbf{y}) + (2\pi)\mathbf{m}(\mathbf{x}, \mathbf{y})) \quad (5.6)$$

5.2 系统校准

5.2.1 摩尔波长的计算

计算每个相位映射可以使用系统校准的过程（第三章有详细介绍）。一个平面薄板安装在平移台上，朝着计算机-投影仪面移动到已知位置（深度或者高度已知）。在每一个位置，和测量物体测量相同的条纹投影到薄板上。之后，计算机镜头捕捉一副图片。对于每一个平板的位置，一个和所捕捉到的图片频率相同的电脑合成的条纹在电脑处理后端叠加到所捕捉到的图片上形成摩尔图样。（所有位置）生成的摩尔图样通过过滤去除高频条纹并提取纯摩尔图样。在同一像素点的强度根据所有平板位置（深度）记录。对于每一个像素点，摩尔条纹的强度随着薄板的移动，遵循一个近似正弦函数的变化。摩尔波长可以通过可以有两个连续的极大（亮条纹）和两个连续的极小值（暗条纹）分别得到。一般认为在两个连续的摩尔条纹中 λ 是常数；但是摩尔波长随着校对深度的增加而递减。为了确定摩尔波长是高度的函数，摩尔波长首先通过在不同薄板位置的每一对连续的波峰的记录下的强度计算。然后对所有像素平均得出不同薄板位置（高度）的不同波峰对平均摩尔波长。最后，摩尔波长作为高度的函数可以通过不同波峰对的所有平均摩尔波长线性拟合得到。多次捕捉图片仅仅只在系统校准阶段使用需要，在物体测量是不需要。为了计算外差法的时间相位展开，需要多个相位映射，根据之前的测量深度的对应的波长可以用来计算每一个相位映射。

5.2.2 X-Y 平面的校准

为了实现 X-Y 平面的校准，由像素坐标到真实世界的坐标的对应使用类似于第三章的方法计算。但一个改进后的方法可以用来在每一个高度（深度，Z 轴）精调比例参数：

$$(P_x)_z = \frac{W}{(N_x)_x}, \quad (P_y)_z = \frac{L}{(N_y)_z} \quad (5.7)$$

其中 $(N_x)_z$ 和 $(N_y)_z$ 是对应真正宽度 W 和真正长度 L 已知几何参数物体的像素个数， $(P_x)_z$ 和 $(P_y)_z$ 分别是在不同深度调整后的比例参数。参考薄板的 $(N_x)_z$ 和 $(N_y)_z$ 可以通过使用在不同高度（深度）位置在摩尔波长系统校准过程得到的同一张图片确定。

5.3 数字摩尔时间相位展开

5.3.1 双波长相位展开

对于双波长的数字摩尔时间相位展开，两个不同频率的条纹投影到物体表面，每一次投影抓拍一个图片。通过数字相位移动，一个电脑合成的条纹和所抓拍图片叠加，产生相位移动的摩尔图样，之后经历第四章描述的条纹去除。然后，相位移动分析计算出两个不同的摩尔波长 λ_1 和 λ_2 的折叠相位 Φ_1 , Φ_2 。在条纹投影测量法 (Fringe Projection Profilometry) 中，至少需要捕捉六张图片来展开时间相位展开，但是在本研究中，只需要捕捉两张图片。每一各摩尔图样的波长 λ_1 , λ_2 按照第三章介绍，在校准阶段计算。

从相位映射 Φ_1 和 Φ_2 ，一个展开的连续的相位 Φ_{12} 和展开的波长 λ_{12} ，其中 $\lambda_{12} = \frac{\lambda_1 \lambda_2}{|\lambda_1 - \lambda_2|}$ ，展开相位是

$$\Phi_{12}(x, y) = \begin{cases} \Phi_1(x, y) - \Phi_2(x, y) & \Phi_1 > \Phi_2 \\ \Phi_1(x, y) - \Phi_2(x, y) + 2\pi & \text{除以上情况以外} \end{cases} \quad (5.9)$$

在这里，拍频波长 λ_{12} 足够大能覆盖被测物体的高度 $h(x, y)$ 的值域。（例如，连续的灰度梯度，在 Φ_{12} 中没有出现相位不确定）。为了最小化噪声引起的相位错误， Φ_{12} 作为参考展开相位映射 Φ_1 , Φ_1 有更小的波长 λ_1 ，如下：

$$\varphi(x, y) = \Phi_1(x, y) + (2\pi)\text{Round}\left(\frac{(\lambda_{12}/\lambda_1)\Phi_{12}(x, y) - \Phi_1(x, y)}{2\pi}\right), \quad (5.9)$$

其中 $\varphi(x, y)$ 是展开相位， Round() 函数计算括号内小数最接近整数。如此，一

个好信噪比的展开相位映射 $\varphi(x, y)$ 可以用来在测量中计算物体高度:

$$\mathbf{h}(\mathbf{x}, \mathbf{y}) = \frac{\lambda_1}{2\pi} \varphi(\mathbf{x}, \mathbf{y}) \quad (5.10)$$

5.3.2 三波长相位展开

一个波长较大的折叠的相位映射有少数的相位阶跃但是噪声比较大，但是一个小波长的相位映射会有更多的相位阶跃但是更高的信噪比。在双波长的相位展开，最好的波长可能不能足以符号被测物体深度，留下相位不确定。增大投影条纹的频率能增大波长 λ_1 和 λ_2 ，能帮助拍频波长覆盖整个被测物体深度，但是这会在展开确定的相位映射牺牲信噪比，会使相位展开过程不可靠。

三波长或者多波长外差法，相位展开能进一步增加拍频波长，并不在展开相位部分牺牲信噪比。在三波长数字摩尔时间相位展开中，三个不同频率的条纹投影到被测物体上，每一个投影条纹拍摄一张图像。对应三个波长 λ_1 , λ_2 , λ_3 ($\lambda_3 > \lambda_2 > \lambda_1$)三个折叠的相位 Φ_1 , Φ_2 , Φ_3 可以从三个捕捉的图像计算出来。可以从三个拍频波长 $\lambda_{12} = \frac{\lambda_1 \lambda_2}{|\lambda_1 - \lambda_2|}$, $\lambda_{23} = \frac{\lambda_2 \lambda_3}{|\lambda_{12} - \lambda_{23}|}$, 计算出的三个比例因子 (λ_{12}/λ_2) , (λ_{23}/λ_2) , $(\lambda_{123}/\lambda_2)$ 用来展开相位，使展开相位覆盖被测物体深度范围。展开相位 Φ_{12} 和展开波长 λ_{12} 从相位映射 Φ_1 和 Φ_2 得出，如下：

$$\Phi_{12}(x, y) = \begin{cases} \Phi_1(x, y) - \Phi_2(x, y) & \Phi_1 > \Phi_2 \\ \Phi_1(x, y) - \Phi_2(x, y) + 2\pi & \text{除以上情况以外} \end{cases} \quad (5.11)$$

为了减小 Φ_{12} 的噪声， Φ_{12} 用来作为展开对应波长 λ_2 的相位映射 Φ_2 的参考，这会使得 $\Phi'_{12}(x, y)$ 比 Φ_{12} 有更高的信噪比：

$$\Phi'_{12} = \Phi_2(x, y) + 2\pi \text{Round}\left(\frac{(\lambda_{12}/\lambda_2)\Phi_{12}(x, y) - \Phi_2(x, y)}{2\pi}\right), \quad (5.12)$$

对应波长 λ_{23} 展开的相位 Φ_{23} 使用和计算 Φ_{12} 一样的方法，由相位映射 Φ_2 和 Φ_3 计算得出：

$$\Phi_{23}(x, y) = \begin{cases} \Phi_2(x, y) - \Phi_3(x, y) & \Phi_2 > \Phi_3 \\ \Phi_2(x, y) - \Phi_3(x, y) + 2\pi & \text{除以上情况以外} \end{cases} \quad (5.13)$$

然后为了再一次减小噪声， $\Phi'_{23}(x, y)$ 有比之前计算的 Φ_{23} 更高的信噪比

$$\Phi'_{23} = \Phi_2(x, y) + (2\pi) \text{Round}\left(\frac{(\lambda_{23}/\lambda_2)\Phi_{23}(x, y) - \Phi_2(x, y)}{2\pi}\right) \quad (5.14)$$

对应能覆盖整个物体深度范围的展开波长 λ_{123} 的相位映射 Φ_{123} （例如，在 Φ_{123} 中没有相位不确定）通过相位映射 $\Phi'_{12}(x, y)$ 比和 $\Phi'_{23}(x, y)$ 计算得出：

$$\Phi_{123}(x, y) = \begin{cases} \Phi'_{12}(x, y) - \Phi'_{23}(x, y) & \Phi'_{12} > \Phi'_{23} \\ \Phi'_{12}(x, y) - \Phi'_{23}(x, y) + 2\pi & \text{除以上情况以外} \end{cases} \quad (5.15)$$

最后， Φ_2 的相位展开通过之前的展开连续相位映射 Φ_{123} 计算出来，如下

$$\varphi = \Phi_2(x, y) + (2\pi) \text{Round}\left(\frac{(\lambda_{123}/\lambda_2)\Phi_{123}(x, y) - \Phi_2(x, y)}{2\pi}\right) \quad (5.16)$$

这个高信噪比的相位映射 $\varphi(x, y)$ 可以用来测量物体高度：

$$\mathbf{h}(\mathbf{x}, \mathbf{y}) = \frac{\lambda_2}{2\pi} \varphi(x, y). \quad (5.17)$$

5.4 实验和结果

5.4.1 实验装置

为了展示数字摩尔多波长的时间相位展开，我们通过一系列光学装置进行了实验，装置包括 LCD 投影仪（Panasonic PT-AE7000U）和 2048x2048 分辨率的单色 CCD 照相机。照相机和投影仪之间的夹角大约为 11 度，照相机-投影仪面里物体距离 2.5m。

5.4.2 系统校准

为了计算摩尔条纹的波长，系统校准使用了安装在平移台上的平薄板。平薄板采取了 200 个位置，在 250mm 的校准深度和 0.007mm 的平移精度采用了 1.25mm 间隔。10, 12, 14 像素周期的二值条纹投影到平薄板上，在不同的已知位置找到捕捉三个不同条纹频率的条纹。但是在测量被测物体时无需在不同位置采集不同频率的图像。这一过程仅仅在系统校准过程中需要，来计算摩尔波长。相位移动的摩尔条纹通过数字化的在捕捉到的图片上相移，之后经过在 5.1 节里提到的条纹去除。最后，摩尔波长的计算步骤通过 5.2.1 里提到的方法进行。最后得到的波长是 $\lambda_1 = 21.850\text{mm}$, $\lambda_2 = 26.048\text{mm}$, $\lambda_3 = 30.573\text{mm}$ 分别对应 10, 12, 和 14 像素周期的图片。

5.4.3 测量

物体测量通过将一个在校准过程中使用过的条纹周期的图样投影到物体上，然

后每个图样捕捉一张图片。相位移动的摩尔图样通过数字的在捕捉到的图片上重叠并相位移动上一个和捕捉图片一样条纹频率的条纹图样，之后经过条纹去除。相位移动的分析用来提取每一个对应条纹频率的折叠相位映射 $\Phi(x, y)$ 的折叠相位。之后数字摩尔时间条纹相位展开在一个表面不连续的面具上实现，两个看空间上分离的物品（一个表面不连续的面具，一个侏儒头）和一个双半球物品。

双波长时间相位展开方法，通过投影两个不同的但用在校准过程中的条纹频率的条纹图样和为每一个条纹频率捕捉一张图像，在表面不连续的面具上进行。对于每个条纹频率，一个高频摩尔图样通过数字相位移动得到。纯摩尔图样有条纹去除方法提取。两个折叠的相位映射 Φ_1 和 Φ_2 可以用摩尔波长 λ_1 , λ_2 得到（5.4.2 节）。展开的连续相位映射 Φ_{12} 和可以覆盖整个待测物体深度的拍频波长 $\lambda_{12} = \frac{\lambda_1 \lambda_2}{|\lambda_1 - \lambda_2|} = 135.567\text{mm}$ ，可以从折叠的相位映射 Φ_1 和 Φ_2 计算得到（图 5.1-d , 5.2-d）。

图 5.1 折叠相位计算：a) 投影上 10 像素宽度的二值条纹的面具，b) 由高频条纹图样和摩尔图样形成的图样，c) 经过条纹去除的摩尔条纹，和 d) 折叠相位 Φ_1 。

图 5.2 折叠相位计算：a) 投影上 12 像素宽度的二值条纹的面具，b) 由高频条纹图样和摩尔图样形成的图样，c) 经过条纹去除的摩尔条纹，和 d) 折叠相位 Φ_2 。

图 5.3 a) 有展开拍频率 λ_{12} 展开图样相位映射 Φ_{12} ，b) 展开的相位 φ ，和 c) 测量得到的面具的点云可视化

为了由最小化 Φ_{12} 里的相位错误，没有相位不确定的 Φ_{12} 用来作为展开对应更小波长 λ_1 相位映射 Φ_1 的参考，从而得到展开相位 φ 。结果展现了仅仅捕捉两张图片能够精准 3D 测量（图 5.3c）来获得高信噪比相位映射的能力。

三波长时间相位展开用在两个空间分离的物体上：表面不连续的面具和一个侏儒头。为了适用于侏儒头比面具更大的被测物体深度，通过投射另一个格子线频率更大的条纹图样，可以在不牺牲信噪比的情况下，可以显著增大拍频的波长。因此，三个不同频率的条纹图样投射到物体上，每一条纹图样（10-, 12-, 14-像素周期），分别捕捉一张图样（图 5.4a, 5.5a, 5.6a）。对于每一张条纹频率，带高频条纹的摩尔图样通过数字相移得到，然后通过条纹去除得到纯摩尔条纹（图 5.4c, 5.5c, 5.6c）。

图 5.4 生成摩尔图样：a) 10 像素周期的二值条纹不着的原始捕捉图像，b) 带高频条纹

的摩尔图样, 和 c) 条纹去除的摩尔图样

图 5.5 生成摩尔图样: a) 12 像素周期的二值条纹不着的原始捕捉图像, b) 带高频条纹的摩尔图样, 和 c) 条纹去除的摩尔图样

图 5.6 生成摩尔图样: a) 14 像素周期的二值条纹不着的原始捕捉图像, b) 带高频条纹的摩尔图样, 和 c) 条纹去除的摩尔图样

三个折叠的相位 ϕ_1 , ϕ_2 , 和 ϕ_3 (图 5.7a, 5.7b 和, 5.7c) 使用不同的摩尔波长 λ_1 , λ_2 , 和 λ_3 计算得出 (5.4.2 节)。对应展开拍频波长 $\lambda_{12} = \frac{\lambda_1\lambda_2}{|\lambda_1 - \lambda_2|} = 135.78\text{mm}$ 的展开相位映射 ϕ_{12} 可以使用相位映射 ϕ_1 和 ϕ_2 计算得出。为了减小由 ϕ_{12} 中的噪声所造成的相位误差, ϕ_{12} 可以用来作为展开更小摩尔波长的相位映射 ϕ_2 , 从而得到更高信噪比的相位映射 ϕ'_{12} (图 5.8b)。

图 5.7 折叠相位映射 a) ϕ_1 , b) ϕ_1 , 和 c) ϕ_1

第二张展开相位映射 ϕ_{23} (图 5.9a), 对应展开拍频波长 $\lambda_{23} = \frac{\lambda_2\lambda_3}{|\lambda_2 - \lambda_3|} = 175.986\text{mm}$, 可以通过相位映射 ϕ_2 和 ϕ_3 计算得出。为了减小由 ϕ_{23} 中的噪声所造成的相位误差, ϕ_{23} 可以用来作为展开更小摩尔波长的相位映射 ϕ_2 , 从而得到更高信噪比的相位映射 ϕ'_{23} (图 5.9b)。用[54]中的方法, 是从相位映射 ϕ_{12} (图 5.8a) 和 ϕ_{23} (图 5.9a) 中计算出覆盖了全部被测物体深度的展开的连续相位映射 (图 5.10a), 最后得出一个含有噪声的相位映射 (图 5.10a)。但本篇论文使用了高质量的相位映射 ϕ'_{12} (图 5.9b) 和 ϕ'_{23} (图 5.10b) 计算出对应展开拍频波长 $\lambda_{123} = \frac{\lambda_{12}\lambda_{23}}{|\lambda_{12} - \lambda_{23}|} = 590.269\text{ mm}$ 的具有高信噪比的连续展开相位映射 ϕ_{123} 。最后为了计算出一个更高信噪比的精确展开相位映射, ϕ_{123} 用来作为参考展开具有较小摩尔波长 λ_2 的 ϕ_2 , 来得到具有更高信噪比的展开相位 φ (图 5.10c)。这一高信噪比的展开相位映射的方法使得只用捕捉三张图片就可以精准 3D 测量不连续和多个空间上隔离的物体 (图 5.11)。

图 5.8. 展开相位: a) 对应展开拍频波长 λ_{12} 的 ϕ_{12} , 和 b) 具有更高信噪比的 ϕ'_{12}

图 5.9. 展开相位: a) 对应展开拍频波长 λ_{23} 的 ϕ_{23} , 和 b) 具有更高信噪比的 ϕ'_{23}

图 5.10. 展开连续的相位映射: a) 基于[54]方法由 ϕ_{12} 和 ϕ_{23} 计算得到连续展开相位, 和 b) 由 ϕ'_{12} 和 ϕ'_{23} 计算的, 具有更高信噪比对应展开拍频波长 λ_{123} 的 ϕ'_{23} , 和 c) 展开相位 φ

图 5.11. 测得空间隔离物体面具和侏儒头的点云可视化

为了展示双图片数字摩尔时间相位展开方法的准确性，一个已知半球直径（真实半径 50.80mm）双半球物体和已知球心之间距离（120mm）被测量。为了增大测量的精度和准确性，校准时，采用了比其他物体更小条纹周期的二值条纹投影（在捕捉图像中 8-和 10-像素条纹）。然后计算出对应 8-和 10-像素周期的图片的摩尔波长是 $\lambda_1 = 16.966\text{mm}$, $\lambda_2 = 21.035\text{mm}$ 。之后在半球物体上采用双波长相位展开，投射两个和校准过程中频率相同的二值条纹图样，每一个图样（8-和 10-像素周期条纹）捕捉一张照片。最后使用条纹去除提取摩尔条纹。

图片 5.12. 生产摩尔条纹：a) 由 8-像素周期二值条纹投影得到的原始双半球物体照片，b) 由摩尔条纹和高频条纹重合生成的图像，和 c) 在条纹去除之后得到的摩尔条纹

图片 5.12. 生产摩尔条纹：a) 由 10-像素周期二值条纹投影得到的原始双半球物体照片，b) 由摩尔条纹和高频条纹重合生成的图像，和 c) 在条纹去除之后得到的摩尔条纹

两个折叠的相位 ϕ_1 和 ϕ_2 （图 5.14a, 5.14b）通过摩尔波长 λ_1 和 λ_2 计算得出。展开的连续相位映射 ϕ_{12} （图 5.15a）和能覆盖物体全部深度范围的拍频波长 $\lambda_{12} = \frac{\lambda_1 \lambda_2}{|\lambda_1 - \lambda_2|} = 87.720\text{mm}$ 能从折叠相位 ϕ_1 和 ϕ_2 （图 5.14a 和图 5.14b）。为了减小由 ϕ_{12} 里噪声产生的相位误差，没有相位不确定的 ϕ_{12} 用来展开相位 ϕ_1 参考展开有着更小摩尔波长 λ_1 相位映射 ϕ_1 得到展开的相位映射 φ （图 5.15b）。利用公式（5.10）进行高度测量，之后最小二乘法球拟合，得到测量的 3D 点云数据。（图 5.15c）。最后测得直径为 50.833mm，和 50.738mm，因此 0.33mm 和 0.062mm 的误差。（球拟合的标准差为 0.146mm 和 0.142mm）。两半球之间的球心距离为 119.812mm，具有 0.188mm 的误差。

图 5.14 折叠相位映射：a) ϕ_1 , b) ϕ_2 。

图 5.15 a) 展开拍频波长 λ_{12} 的相位映射 ϕ_{12} , b) 展开的相位 ϕ_{12} , 和 c) 双半球物体的点云可视化

一个真实半球的截面测量点的采样在图 5.16 中可见。测量点在大多数地方很接近真实值。但是，在靠近表面边缘的存在较大误差，这个时候镜头和投影仪的光轴平行于表面。

图 5.16 真实半球和双半球截面测量点采样

5.5 讨论

为了实现数字摩尔的本章讨论了双图片和三图片时间相位展开方法，产生了一个高信噪比的相位映射，因此对于之前的数字摩尔时间相位展开方法是一个改善。在系统校准中计算摩尔波长也使得可以使用有噪声的相位映射作为参考展开更短波长的相位映射。所以，最终能获得一个噪声少，连续精准的相位映射。对于每一个波长，本方法只需要投影一次条纹图样，开展一次时间相位展开。这一新方法所需要捕捉图片的数量较少有助于测量动态的被测物体，无论是移动的还是变形的。

参考文献

- [1] Ryu, Weon-Jae, Young-June Kang, Sung-Hoon Baik, and Shin-Jae Kang. "A study on the 3-D measurement by using digital projection moiré method." Optik-International Journal for Light and Electron Optics 119, no. 10 (2008): 453-458.

附录

(所翻译文献第五章原文)

Chapter 5

Two-image and three-image temporal phase unwrapping

In this chapter, two-image and three-image digital-moiré temporal phase unwrapping were developed to compute an accurate continuous phase map using projection of two and three grid patterns of different frequencies, respectively. The method requires projection of only a single binary grid and capture of a single image for each grid pitch to calculate the wrapped phase map, while phase-shifting is performed digitally in a post-process. The phase-shift analysis results in phase maps with different moiré wavelengths. Calculation of the moiré wavelength for each phase map during the system calibration enables the use of the noisy extended phase map as a reference to unwrap either of the phase maps with the shorter wavelengths. This permits accurate continuous phase map computation using fewer images than for fringe projection methods.

5.1 Digital phase-shifting moiré

The method of temporal phase unwrapping using multi-wavelength digital phase-shifting moiré involves projecting multiple binary grid patterns of different pitch onto the object surface, and capturing only a single image for each projected pattern. Then, for each captured image (of different pitch), a synthetically produced (computer generated) grid of the same pitch as the captured image is overlaid on the captured image and digitally shifted to generate multiple phase-shifted moiré images, as detailed in Chapter 3.

The generated phase-shifted moiré images contain the moiré contours as well as the unwanted high-frequency grid-pattern. Grid removal is then performed to extract pure moiré patterns, as detailed in Chapter 4. The intensity distribution of the phase-shifted moiré patterns after grid removal is described by:

$$I_i(x, y) = a(x, y) + b(x, y)\cos(\Phi(x, y) + \delta_i) , \quad (5.1)$$

where $a(x, y)$ and $b(x, y)$ are intensity background and modulation, respectively, (x, y) are the image coordinates, $\Phi(x, y)$ is the phase map that contains object height information, and $\delta_i = 2\pi i/N$ are the phase-shifts between images. To calculate the phase map $\Phi(x, y)$, at least three images ($N=3$) of phase-shifted moiré patterns are required:

$$\Phi(x, y) = -\tan^{-1} \left(\frac{\sum_{i=1}^N I_i(x, y) \sin \delta_i}{\sum_{i=1}^N I_i(x, y) \cos \delta_i} \right), i = 1, 2, \dots, N. \quad (5.2)$$

Because of the arctan function in Eq. 5.2, the computed phase $\Phi(x, y)$ is wrapped in the range $[-\pi, \pi]$, and a 2D phase unwrapping technique is required to calculate a continuous phase map $\varphi(x, y)$. This process removes the 2π ambiguities of the wrapped phase according to the fringe order $m(x, y)$.

$$\varphi(x, y) = \Phi(x, y) + (2\pi)m(x, y). \quad (5.3)$$

The relationship between the computed unwrapped phase $\varphi(x, y)$ and object height h depends on the system-geometry parameters and can be expressed as follows:

$$h(x, y) = K\varphi(x, y). \quad (5.4)$$

The coefficient K is a function of the moiré-wavelength λ :

$$K = \frac{\lambda}{2\pi}. \quad (5.5)$$

Eq. (5.4) can thus be rewritten as:

$$h(x, y) = \frac{\lambda}{2\pi} (\Phi(x, y) + (2\pi)m(x, y)). \quad (5.6)$$

5.2 System calibration

5.2.1 Computation of the moiré wavelength

Computation of the moiré wavelength λ for each phase map can be performed in a system calibration process as follows (detailed in Chapter 3). A flat plate is mounted on a translation stage and moved toward the camera-projector plane to several known positions (depths or heights). At each position, the same grid pattern used during object measurement is projected onto the plate and an image is captured. For each plate position, a computer-generated grid pattern of the same pitch as in the captured image, is digitally superimposed onto the captured image to generate a moiré pattern. The generated images (for all positions) are filtered to remove the high frequency grid and extract pure moiré patterns. The intensity at a single pixel is tracked across all plate positions (over depth). For every pixel, the moiré fringe intensities across plate positions follow a near-sinusoidal function of the plate translation. The moiré wavelength can be estimated by the distance between two successive maxima (bright fringes) or two successive

minima (dark fringes), respectively. It is common to assume that λ is constant between successive moiré fringes; however, the moiré wavelength decreases with increasing calibration depth. To determine the moiré wavelength as a function of height, the moiré wavelength is first computed at each pair of successive peaks from the tracked intensities over plate positions. The average moiré wavelength over all pixels is then computed at the different peak pairs corresponding to different plate positions (heights). Finally, the moiré wavelength as a function of height is approximated by a line fit to all average moiré wavelengths computed at different peak pairs. The capture of multiple images is only required during system calibration, and not during object measurement. To perform heterodyne temporal phase unwrapping, multiple phase maps are required, and the wavelength corresponding to the middle calibration depth is used for each phase map.

5.2.2 X-Y plane calibration

To perform X - Y plane calibration, the mapping of pixel coordinates to real world coordinates is computed using a method similar to that in Chapter 3. However, a modified method is used to refine the scaling parameters at each height (depth, Z axis);

$$(P_x)_z = \frac{W}{(N_x)_z}, \quad (P_y)_z = \frac{L}{(N_y)_z}. \quad (5.7)$$

where, $(N_x)_z$ and $(N_y)_z$ are the number of pixels in the captured image corresponding to the true width W and length L of the object of known geometry, and $(P_x)_z$ and $(P_y)_z$ are the refined scaling parameters, respectively, at each depth. $(N_x)_z$ and $(N_y)_z$ for the reference plate were determined at multiple height (depth) positions using the same images obtained during the system calibration for moiré wavelength.

5.3 Digital-moiré temporal phase unwrapping

5.3.1 Two-wavelength phase-unwrapping

For two-wavelength digital-moiré temporal phase-unwrapping, two fringe patterns of different pitch are projected onto the object surface and a single image is captured for each projected pattern. Phase-shifted moiré patterns (images) are generated by digitally phase shifting a computer-generated grid overlaid on the captured images, followed by grid removal, described in Chapter 4. Phase shift analysis is then applied to compute two wrapped phase maps Φ_1 , Φ_2 with

different moiré wavelengths λ_1, λ_2 ($\lambda_2 > \lambda_1$). In FPP techniques, at least six captured images are needed to perform two-frequency temporal phase unwrapping, while in this research, only two captured images are required. The moiré wavelength of each moiré pattern λ_1, λ_2 , are calculated in the calibration stage, as explained in Chapter 3.

From phase maps Φ_1 and Φ_2 , an extended continuous phase map Φ_{12} with extended wavelength λ_{12} , where $\lambda_{12} = \frac{\lambda_1\lambda_2}{|\lambda_1 - \lambda_2|}$, is then calculated:

$$\Phi_{12}(x, y) = \begin{cases} \Phi_1(x, y) - \Phi_2(x, y), & \Phi_1 > \Phi_2 \\ \Phi_1(x, y) - \Phi_2(x, y) + 2\pi, & \text{otherwise} \end{cases} \quad (5.8)$$

Here, the beat wavelength λ_{12} is large enough to cover the entire range of the object's depth $h(x, y)$ (i.e. continuous gray level gradient, no phase ambiguity in Φ_{12}). To minimize the phase error caused by noise, Φ_{12} can be used as a reference to unwrap the phase map Φ_1 , which has the lower wavelength λ_1 , as follows:

$$\varphi(x, y) = \Phi_1(x, y) + (2\pi)\text{Round}\left(\frac{(\lambda_{12}/\lambda_1)\Phi_{12}(x, y) - \Phi_1(x, y)}{2\pi}\right), \quad (5.9)$$

where $\varphi(x, y)$ is the unwrapped phase map and $\text{Round}(\)$ computes the closest integer value. This high-SNR unwrapped phase map $\varphi(x, y)$ can then be used during measurement to calculate the object height:

$$h(x, y) = \frac{\lambda_1}{2\pi} \varphi(x, y). \quad (5.10)$$

5.3.2 Three-wavelength phase-unwrapping

A wrapped phase map with large wavelength has few phase jumps but tends to be noisy, while a phase map with smaller wavelength has more phase jumps, but higher SNR. In two-wavelength phase unwrapping the beat wavelength may not be sufficient to cover the entire object depth, leaving phase ambiguity. Increasing the pitch of projected patterns to enlarge the wavelengths λ_1 and λ_2 , may help the beat wavelength to cover the entire object depth; however, this sacrifices SNR in the extended unambiguous phase map, which makes the phase unwrapping process unreliable.

Three-wavelength or multi-wavelength heterodyne phase-unwrapping can further increase the beat wavelength without sacrificing SNR in the extended phase map. In three-wavelength digital-moiré temporal phase-unwrapping, three fringe patterns of different pitch are projected onto the object and a single image is captured for each projected pattern. Three wrapped phase maps Φ_1 , Φ_2 , Φ_3 with different wavelengths λ_1 , λ_2 , λ_3 , ($\lambda_3 > \lambda_2 > \lambda_1$) are computed using only three captured images. Three scale factors (λ_{12}/λ_2) , (λ_{23}/λ_2) , and $(\lambda_{123}/\lambda_2)$ from three beat wavelengths, $\lambda_{12} = \frac{\lambda_1\lambda_2}{|\lambda_1-\lambda_2|}$, $\lambda_{23} = \frac{\lambda_2\lambda_3}{|\lambda_2-\lambda_3|}$, and $\lambda_{123} = \frac{\lambda_{12}\lambda_{23}}{|\lambda_{12}-\lambda_{23}|}$ are used in the phase unwrapping process to produce an extended continuous phase map that covers the entire object range of depth. An extended phase map Φ_{12} with extended wavelength λ_{12} , is computed from phase maps Φ_1 and Φ_2 as follows:

$$\Phi_{12}(x, y) = \begin{cases} \Phi_1(x, y) - \Phi_2(x, y), & \Phi_1 > \Phi_2 \\ \Phi_1(x, y) - \Phi_2(x, y) + 2\pi, & \text{otherwise} \end{cases} . \quad (5.11)$$

To minimize the noise in Φ_{12} , Φ_{12} is used as a reference to unwrap the phase map Φ_2 with wavelength λ_2 , which results in $\Phi'_{12}(x, y)$ with higher SNR than Φ_{12} :

$$\Phi'_{12}(x, y) = \Phi_2(x, y) + (2\pi)\text{Round}\left(\frac{(\lambda_{12}/\lambda_2)\Phi_{12}(x, y) - \Phi_2(x, y)}{2\pi}\right), \quad (5.12)$$

An extended phase map Φ_{23} with extended wavelength λ_{23} , is computed from phase maps Φ_2 and Φ_3 in a similar manner to Φ_{12} :

$$\Phi_{23}(x, y) = \begin{cases} \Phi_2(x, y) - \Phi_3(x, y), & \Phi_2 > \Phi_3 \\ \Phi_2(x, y) - \Phi_3(x, y) + 2\pi, & \text{otherwise} \end{cases} . \quad (5.13)$$

Again to minimize noise, $\Phi'_{23}(x, y)$ with higher SNR than Φ_{23} is calculated as follows:

$$\Phi'_{23}(x, y) = \Phi_2(x, y) + (2\pi)\text{Round}\left(\frac{(\lambda_{23}/\lambda_2)\Phi_{23}(x, y) - \Phi_2(x, y)}{2\pi}\right), \quad (5.14)$$

The extended continuous phase map Φ_{123} with extended wavelength λ_{123} that covers the entire object range of depth $h(x, y)$ (i.e. no phase ambiguity in Φ_{123}), is computed from phase maps $\Phi'_{12}(x, y)$ and $\Phi'_{23}(x, y)$:

$$\Phi_{123}(x, y) = \begin{cases} \Phi'_{12}(x, y) - \Phi'_{23}(x, y), & \Phi'_{12} > \Phi'_{23} \\ \Phi'_{12}(x, y) - \Phi'_{23}(x, y) + 2\pi, & \text{otherwise} \end{cases} \quad (5.15)$$

Finally, the phase unwrapping of Φ_2 is performed using the extended continuous phase map $\Phi_{123}(x, y)$ as follows:

$$\varphi(x, y) = \Phi_2(x, y) + (2\pi)\text{Round}\left(\frac{(\lambda_{123}/\lambda_2)\Phi_{123}(x, y) - \Phi_2(x, y)}{2\pi}\right), \quad (5.16)$$

This high-SNR unwrapped phase map $\varphi(x, y)$ can then be used during measurement to calculate the object height:

$$h(x, y) = \frac{\lambda_2}{2\pi} \varphi(x, y) . \quad (5.17)$$

5.4 Experiments and Results

5.4.1 Experimental setup

To demonstrate the method of digital-moiré multi-wavelength temporal phase unwrapping, experiments were performed using an optical setup including a LCD projector (Panasonic PT-AE7000U) and monochrome CCD camera 2048 x 2048 resolution, with approximately 11 deg camera-projector angle, and 2.5 m camera-projector-plane to object distance.

5.4.2 System Calibration

To calculate the moiré wavelengths, system calibration was performed using a flat plate mounted on a linear translation stage and translated to 200 positions in 1.25 mm increments over a 250 mm calibration depth with 0.007 mm translation precision. Three binary grid patterns with different grid pitches were projected onto the flat plate and three images with 10, 12, and 14-pixel grid-pitches, respectively, were captured at each of the different known plate positions. The capture of multiple images at different known positions is not required during object measurement, but was required during system calibration to calculate the moiré wavelengths. Phase-shifted moiré patterns (images) were generated by digitally phase shifting a computer-generated grid overlaid on the captured images, followed by grid removal, as described in Section 5.1. Finally, the procedure of moiré wavelength calculation was performed as described in Section 5.2.1 and the resulting moiré wavelengths were $\lambda_1 = 21.850$ mm, $\lambda_2 = 26.048$ mm, and $\lambda_3 = 30.573$ mm for the 10, 12, and 14-pixel-pitch images, respectively.

5.4.3 Measurement

Object measurements were performed by projecting onto the object a single grid pattern for each grid pitch used in the calibration, and capturing a single image for each pattern. Phase-shifted moiré patterns (images) were generated by digitally phase shifting a computer-generated grid of the same pitch as the captured image overlaid on the captured images, followed by grid removal. Phase-shift analysis was applied to extract the wrapped phase map $\Phi(x, y)$ for each grid pitch. The digital moiré temporal phase unwrapping method was performed on a mask with surface discontinuities, two spatially isolated objects (a mask with surface discontinuities and a manikin head) and a double-hemispherical object.

Two-wavelength temporal phase unwrapping was applied to the mask with surface discontinuities by projecting two binary grid patterns with the grid pitches used in the calibration, and capturing a single image for each pattern (10- and 12-pixel grid pitch) (Figs. 5.1a, 5.2a). For each grid pitch, a moiré pattern with high-frequency grid lines was generated by digital phase-shifting moiré (Figs. 5.1b, 5.2b), and a pure moiré pattern was extracted by grid removal (Figs. 5.1c, 5.2c). Two wrapped phase maps Φ_1 and Φ_2 (Figs. 5.1d, 5.2d) were computed with moiré wavelengths λ_1 and λ_2 (Section 5.4.2). The extended continuous phase map Φ_{12} (Fig. 5.3a) with extended beat wavelength $\lambda_{12} = \frac{\lambda_1\lambda_2}{|\lambda_1 - \lambda_2|} = 135.567$ mm, which covers the entire range of depth, was computed from wrapped phase maps Φ_1 and Φ_2 (Figs. 5.1d, 5.2d).

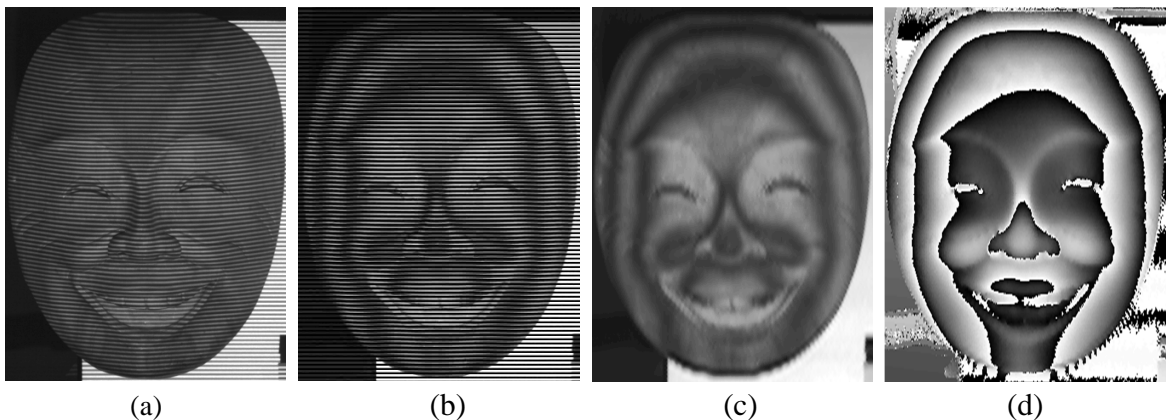


Figure 5.1. Wrapped phase map computation: a) original captured image of the mask with binary grid of 10-pixel pitch, b) generated image with moiré pattern and high-frequency grid lines, c) moiré pattern after grid removal, and d) wrapped phase map Φ_1 .

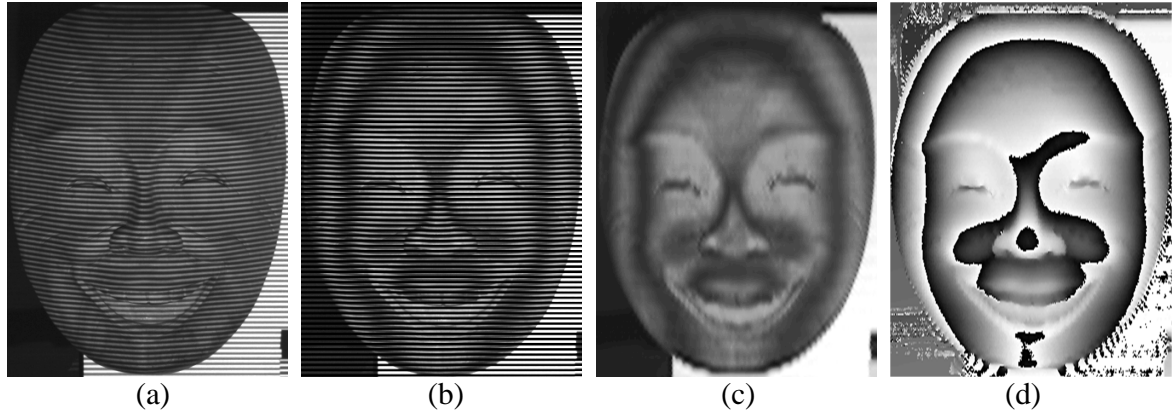


Figure 5.2. Wrapped phase map computation: a) original captured image of the mask with binary grid of 12-pixel pitch, b) generated image with moiré pattern and high-frequency grid lines, c) moiré pattern after grid removal, and d) wrapped phase map Φ_2 .

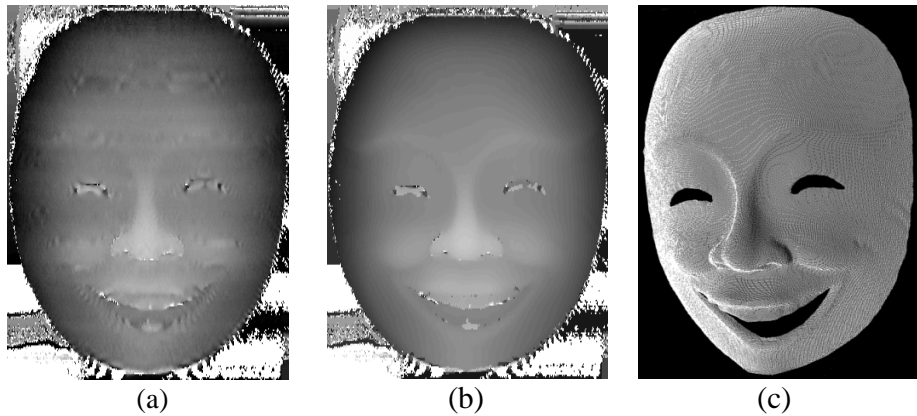


Figure 5.3. a) Extended continuous phase map Φ_{12} with extended beat wavelength λ_{12} , b) unwrapped phase map φ , and c) point cloud representation of measured points of mask.

To minimize the phase error caused by the noise in Φ_{12} , Φ_{12} with no phase ambiguity was used as a reference to unwrap the phase map Φ_1 with smaller moiré wavelength λ_1 , to obtain the unwrapped phase map φ (Fig. 5.3b). The result demonstrates the ability to obtain an unwrapped phase map with high SNR to perform accurate 3D measurement (Fig. 5.3c) of objects with discontinuities, using only two captured images.

Three-wavelength temporal phase unwrapping was applied to two spatially isolated objects: a mask with surface discontinuities and a manikin head. To handle the greater depth of the manikin compared to the mask, the beat wavelength was increased without sacrificing SNR in the extended phase map, by projection of another pattern with greater grid pitch. Thus, three binary grid patterns with different grid pitches were projected onto the objects and a single image

was captured for each pattern (10-, 12-, and 14-pixel grid pitch) (Figs. 5.4a, 5.5a, and 5.6a). For each grid pitch, a moiré pattern with high-frequency grid lines was generated by digital phase-shifting moiré (Figs. 5.4b, 5.5b, and 5.6b) and a pure moiré pattern was extracted by grid removal (Figs. 5.4c, 5.5c and 5.6c).

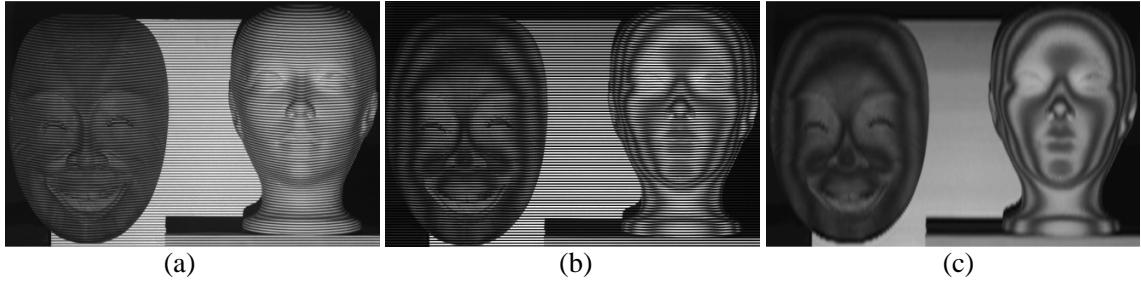


Figure 5.4. Moiré pattern generation: a) original captured image of objects with binary grid of 10-pixel pitch, b) generated image with moiré pattern and high-frequency grid lines, and c) moiré pattern after grid removal.

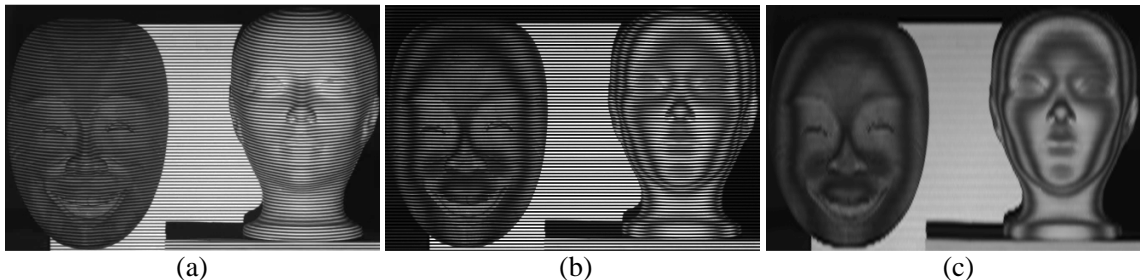


Figure 5.5. Moiré pattern generation: a) original captured image of objects with binary grid of 12-pixel pitch, b) generated image with moiré pattern and high-frequency grid lines, and c) moiré pattern after grid removal.

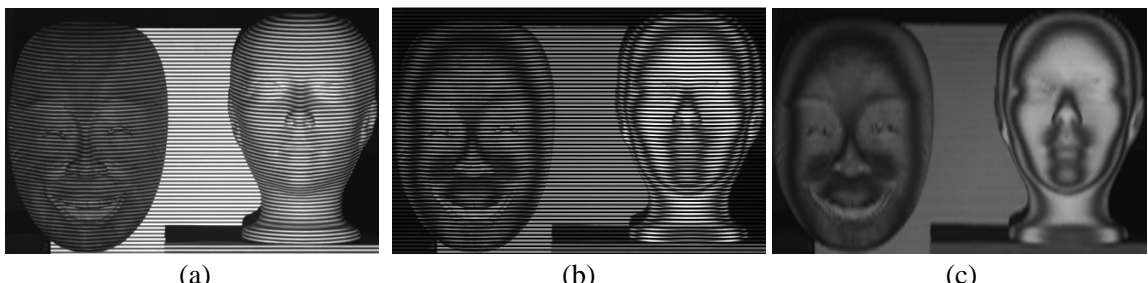


Figure 5.6. Moiré pattern generation: a) original captured image of objects with binary grid of 14-pixel pitch, b) generated image with moiré pattern and high-frequency grid lines, and c) moiré pattern after grid removal.

Three wrapped phase maps Φ_1 , Φ_2 , and Φ_3 (Figs. 5.7a, 5.7b and 5.7c) were computed with different moiré wavelengths λ_1 , λ_2 , and λ_3 (Section 5.4.2). The extended phase map Φ_{12} (Fig. 5.8a) with extended beat wavelength $\lambda_{12} = \frac{\lambda_1\lambda_2}{|\lambda_1-\lambda_2|} = 135.567$ mm was computed from phase maps Φ_1 and Φ_2 . To minimize the phase error caused by the noise in Φ_{12} , Φ_{12} was used as a reference to unwrap the phase map Φ_2 with smaller moiré wavelength λ_2 , to obtain the phase map Φ'_{12} (Fig. 5.8b) with higher SNR.

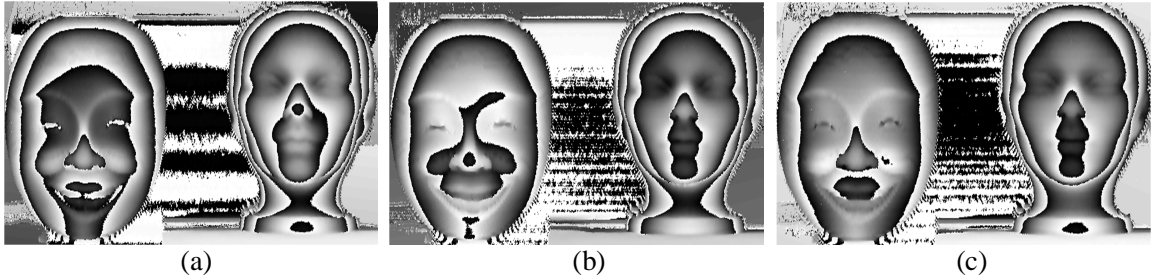


Figure 5.7. Wrapped phase maps a) Φ_1 , b) Φ_2 , and c) Φ_3

A second extended phase map Φ_{23} (Fig. 5.9a) with extended beat wavelength $\lambda_{23} = \frac{\lambda_2\lambda_3}{|\lambda_2-\lambda_3|} = 175.986$ mm was computed from phase maps Φ_2 and Φ_3 . To minimize the phase error caused by the noise in Φ_{23} , Φ_{23} was used as a reference to unwrap the phase map Φ_2 with smaller moiré wavelength λ_2 , to obtain the phase map Φ'_{23} (Fig. 5.9b) with higher SNR. Using the method in [54], the extended continuous phase map (Fig. 5.10a), which covers the entire range of depth, was computed from phase maps Φ_{12} (Fig. 5.8a) and Φ_{23} (Fig. 5.9a), resulting in a noisy phase map (Fig. 5.10a). The extended continuous phase map with high SNR Φ_{123} (Fig. 5.10b) with extended beat wavelength $\lambda_{123} = \frac{\lambda_{12}\lambda_{23}}{|\lambda_{12}-\lambda_{23}|} = 590.269$ mm was calculated from high quality phase maps Φ'_{12} (Fig. 5.8b) and Φ'_{23} (Fig. 5.9b). Finally, to calculate a more accurate unwrapped phase map with high SNR, Φ_{123} was used as a reference to unwrap Φ_2 with smaller moiré wavelength λ_2 , to obtain the unwrapped phase map φ (Fig. 5.10c), which has high SNR. This high-SNR unwrapped phase map enables accurate 3D measurement of objects with discontinuities and multiple spatially-isolated objects (Fig. 5.11) using only three captured images.

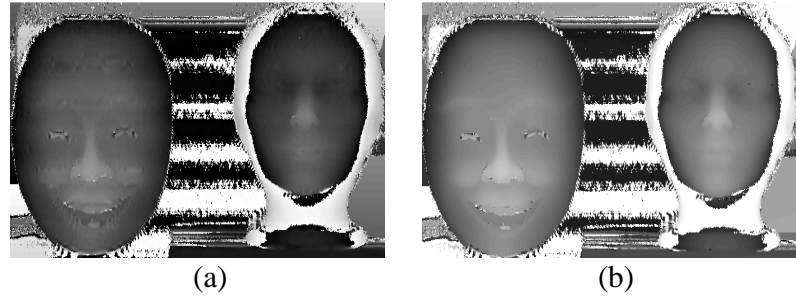


Figure 5.8. Extended phase maps: a) Φ_{12} with extended beat wavelength λ_{12} , and b) Φ'_{12} with higher SNR.

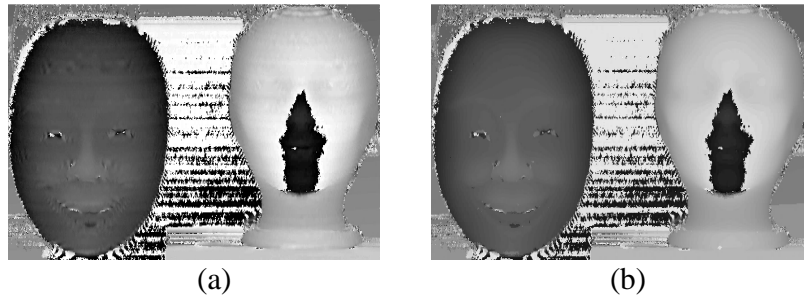


Figure 5.9. Extended phase maps: a) Φ_{23} with extended beat wavelength λ_{23} , and b) Φ'_{23} with higher SNR.

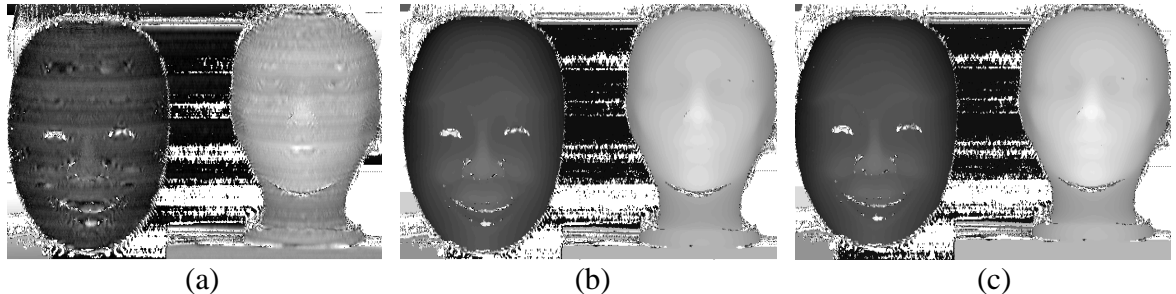


Figure 5.10. Extended continuous phase maps: a) extended continuous phase map based on [54] calculated from Φ_{12} and Φ_{23} , b) Φ_{123} with high SNR and with extended beat wavelength λ_{123} calculated from Φ'_{12} and Φ'_{23} , and c) unwrapped phase map φ .

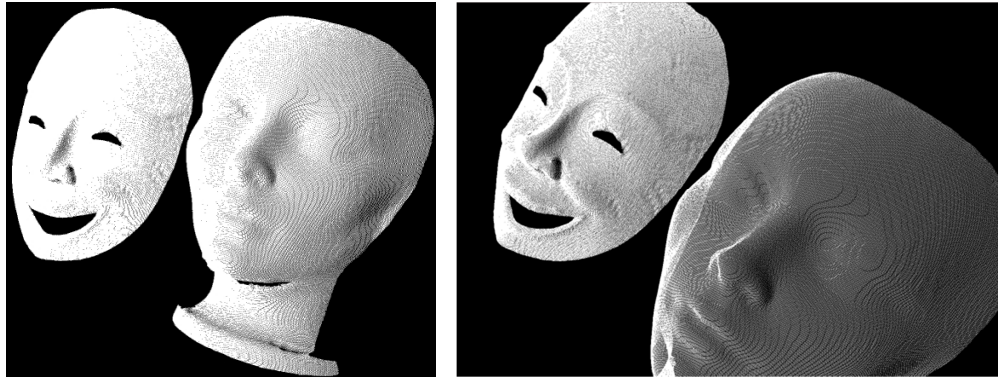


Figure 5.11. Point cloud representations of measured points of spatially isolated objects, mask and manikin head.

To demonstrate the measurement accuracy of the two-image digital-moiré temporal phase unwrapping method, a double-hemispherical object with known radii of two hemispheres (true radius 50.80 mm) and known distance between the centers (120 mm) was measured. To increase the measurement resolution and accuracy, the calibration was performed by projecting two binary grid patterns with smaller grid pitches (resulting in 8- and 10-pixel grid pitch in the captured images) than for the other objects. Moiré wavelength calculation was performed and yielded moiré wavelengths $\lambda_1 = 16.966$ mm and $\lambda_2 = 21.035$ mm for the 8- and 10-pixel-pitch images, respectively. Two-wavelength temporal phase unwrapping was applied to the double-hemispherical object by projecting two binary grid patterns with the grid pitches used in the calibration, and capturing a single image for each pattern (8- and 10-pixel grid pitch) (Figs. 5.12a, 5.13a). For each grid pitch, a moiré pattern with high-frequency grid lines was generated by digital phase-shifting moiré (Figs. 5.12b, 5.13b), and a moiré pattern was extracted by grid removal (Figs. 5.12c, 5.13c).

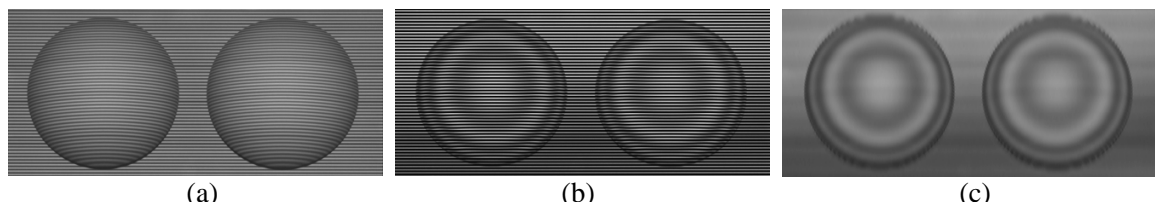


Figure 5.12. Moiré pattern generation: a) original captured image of double hemispherical object with binary grid of 8-pixel pitch, b) generated image with moiré pattern and high-frequency grid lines, and c) moiré pattern after grid removal.

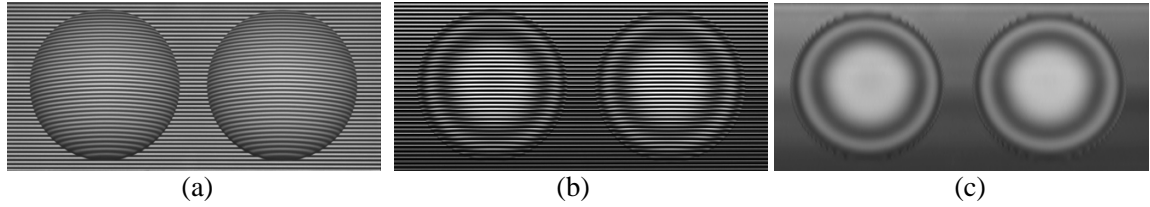


Figure 5.13. Moiré pattern generation: a) original captured image of double hemispherical object with binary grid of 10-pixel pitch, b) generated image with moiré pattern and high-frequency grid lines, and c) moiré pattern after grid removal.

Two wrapped phase maps Φ_1 and Φ_2 (Figs. 5.14a, 5.14b) were computed with moiré wavelengths λ_1 and λ_2 . The extended continuous phase map Φ_{12} (Fig. 5.15a) with extended beat wavelength $\lambda_{12} = \frac{\lambda_1\lambda_2}{|\lambda_1-\lambda_2|} = 87.720$ mm, which covers the entire range of depth, was computed from wrapped phase maps Φ_1 and Φ_2 (Figs. 5.14a and 5.14b). To minimize the phase error caused by the noise in Φ_{12} , Φ_{12} with no phase ambiguity was used as a reference to unwrap the phase map Φ_1 with smaller moiré wavelength λ_1 , to obtain the unwrapped phase map φ (Fig. 5.15b). Height measurement was performed using Eq. (5.10) and least-squares fitted spheres to the measured 3D point cloud data (Fig. 5.15c) had radii of 50.833 mm and 50.738 mm, and thus errors of 0.033 mm and 0.062 mm, respectively (sphere fitting standard deviations were 0.146 mm and 0.142 mm). Centre-to-centre distance between hemispheres was 119.812 mm, thus with an error of 0.188 mm.

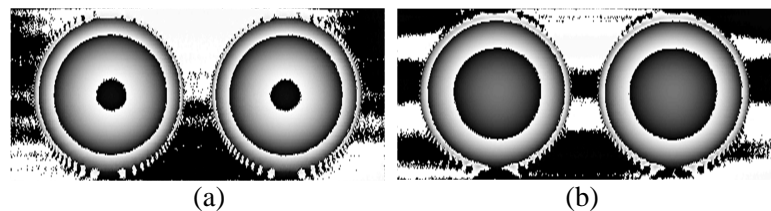


Figure 5.14. Wrapped phase maps: a) Φ_1 , b) Φ_2 .

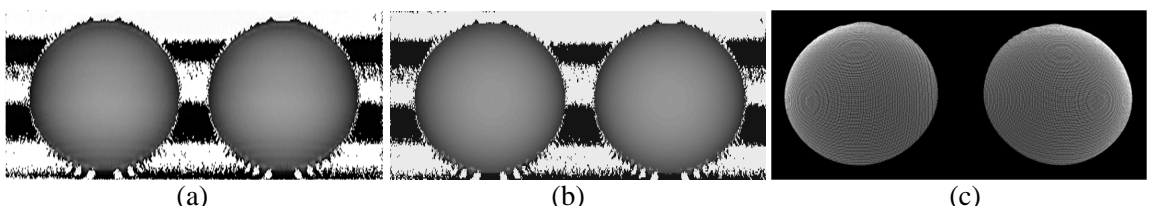


Figure 5.15. a) Extended continuous phase map Φ_{12} with extended beat wavelength λ_{12} , b) unwrapped phase map φ , and c) point cloud representation of double hemispherical object.

A sample cross-section of measured points with the true semicircles is shown in Fig. 5.16, The measured points are close to the true values for most of the surface. As commonly occurring, larger errors are seen near the edge of the surface, where the camera and projector optical axes are nearly parallel to the surface.

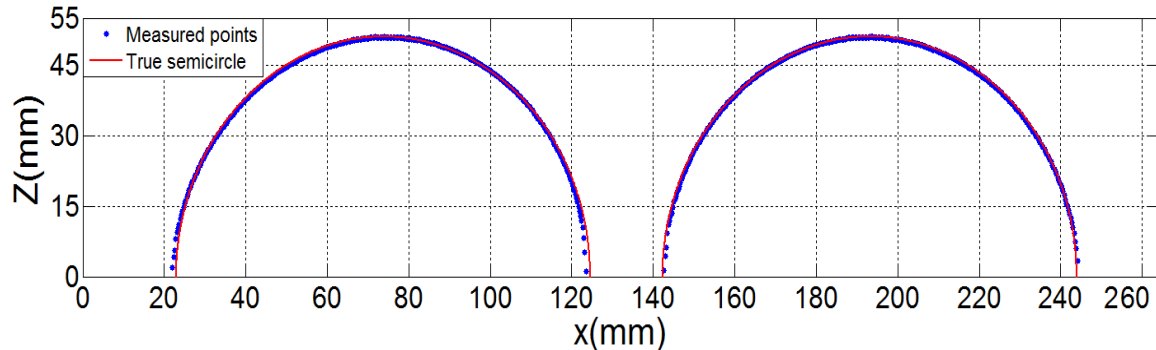


Figure 5.16. Sample cross-section of measured points of double hemispherical object and true semicircles.

5.5 Discussion

Two-image and three-image temporal phase unwrapping, developed in this chapter for digital moiré, yields a high-SNR unwrapped phase map and is thus an improvement over previous temporal phase unwrapping for digital moiré. Moiré wavelength calculation during the system calibration provides an ability to use the extended noisy phase map as a reference to unwrap the phase map with shorter wavelength, and thus achieve a less noisy and more accurate continuous phase map. Only a single pattern has to be projected and thus single image captured to compute each phase map with different wavelength to perform temporal phase unwrapping by digital moiré. The number of captured images required by this new method is one third that for three-wavelength heterodyne temporal phase unwrapping by fringe projection techniques. Decreasing the number of required captured images would be advantageous in measuring dynamic objects, either moving or deforming.

6.2 Limitations and Future Work

1. For the techniques developed in this research, a reference plate is required during object surface measurement. Encoding a marker or colour-stripe in the projected pattern as in [85, 86] might avoid the need for the reference plate, and thus simplify the measurement setup.

Recommended future work would be to:

- Devise a new technique or new projection pattern to perform absolute measurement of objects without requiring the reference plate during measurement:

2. The developed grid removal technique based on SWT-FFT requires adjusting of two parameters: the decomposition level of the wavelet transform and the damping factor of the Gaussian function in the Fourier transform. The decomposition level depends on the pitch of the captured grid on the object surface and the damping factor depends on the curvature of the grid. The damping factor and decomposition level have to be as small as possible to keep the useful information unchanged, but large enough to remove the high frequency grids.

Recommended future work would be to:

- Make the grid removal technique automatic by detecting the pitch and curvature of the image-captured grid lines, and adjusting the decomposition level and the damping factor accordingly as described above. This could permit automatic grid removal and thus allow automated measurement.
3. The developed system calibration technique only performs phase-to-height mapping and requires separate X-Y plane calibration.

Recommended future work would be to:

- Develop a new calibration technique that combines stereo-vision [43-45] (using two cameras and one projector) with digital moiré. This could allow the 3D coordinates of the object surface to be computed from 2D image coordinates based on well-known established techniques for stereo cameras. This combination may allow the use of moiré patterns to aid determination of the correspondence between camera images and to use the intrinsic (camera optics) and extrinsic (system geometry) parameters in measurement as for stereo cameras. In another approach, the system calibration might be performed using a single camera projector system [45], where the